Cement and Concrete Research 203 (2026) 108185

Contents lists available at ScienceDirect

Cement and Concrete Research

journal homepage: www.elsevier.com/locate/cemconres

Potential and challenges of *in situ* ATR-FTIR spectroscopy in the analysis of cement hydration: Combined evaluation with *in-situ* and *ex-situ* XRD

Angela Ullrich [a,*], Krassimir Garbev [a], Peter Stemmermann [a]

[a] *Institute for Technical Chemistry, Karlsruhe Institute of Technology, Hermann-von-Helmholtz-Platz 1, 76344, Eggenstein-Leopoldshafen, Germany*

ARTICLE INFO

Keywords:
ATR spectroscopy
Cement hydration
In situ
X-ray diffraction
C-S-H

ABSTRACT

The core of this study is the detailed investigation of early age cement hydration by ATR-FTIR spectroscopy. Spectra were obtained *in situ* on a CEM I 52.5R during the first 24 h of hydration. The data is discussed in conjunction with the quantitative phase contents obtained by *in situ* and *ex situ* X-ray diffraction. Cement pastes with water-to-cement ratios of 0.3, 0.37, and 0.45 are compared with regard to suitability for the method and the influence of water content on reaction kinetics. In addition, different data evaluation methods are compared with respect to outcome and effort. Whereas the determination of characteristic integral areas proves to be sufficient for qualitative tracking of water consumption and the formation of hydration products like C-S-H and ettringite (AFt), detailed peak fitting provides additional information on the variation of overlaying peaks during raw material consumption and product formation and reveals structural changes within individual phases.

1. Introduction

Although numerous theories and thermodynamic models have been developed to explain the process of cement hydration, they still rely heavily on experimental data [1,2]. In the past, major progress has been achieved, for example, in the modelling of water activity and the dynamic microstructure, but there is still a lack of data on the way towards quantitative models. Hydration kinetics and hydrated phase assemblages were studied routinely by calorimetry, thermal analysis, scanning electron microscopy, NMR, and X-ray diffraction [3,4,5,6]. Nevertheless, a major obstacle is the lack of routine methods for the examination of early cement hydration.

As *in situ* X-ray diffraction is generally conducted without the addition of a standard, it accounts only for the crystalline phases. The main binding phase in cements, calcium-silicate-hydrate (C-S-H), which is poorly crystalline and X-ray amorphous, is not directly detectable. Hence, full phase quantification is mostly restricted to measurements of the raw material and the product after the hydration experiment. In addition to qualitative *in-situ* or quantitative *ex situ* determination of phase composition, quantitative *in situ* X-ray diffraction (XRD) proved to be a powerful tool to assess the hydration of individual minerals [7,8]. The K/G-factor method, which is based on the measurement of an external standard [9], not only enables absolute quantification of amorphous and crystalline contents but also offers the possibility to calculate the degree of hydration [10]. However, detailed knowledge of the sample composition is mandatory as the mass absorption coefficient is required. Jansen et al. investigated this method extensively in order to identify sources of error [11]. They achieved a complete mass balance and validated it against heat flow curves and ^{1}H NMR. [12,13,14]. However, the quantity of the C-S-H phase determined by XRD is based on the X-ray amorphous content that also contains residual water and other low crystalline phases like amorphous $CaCO_3$ and CH. Hence, the composition can only be recalculated by mass balance of the crystalline components against the oxide composition. In addition, the detectability of hydration phases is limited by small crystallite sizes, intrinsic disorder, and overlapping of reflections, and finally, it is time-consuming to obtain a powder pattern in a 2theta range reasonable for Rietveld analysis. The use of Bragg-Brentano reflection geometry has an additional drawback of overestimating the quantity of CH due to sample "bleeding" under the protection foil usually used (Kapton, Mylar, *etc.*) and extensive crystallization of hydrated phases on the sample surface during *in situ* XRD measurements. All these facts hamper the tracking of the nucleation and subsequent growth of hydrated phases, especially of C-S-H, in the early stage of hydration.

Spectroscopic methods proved to be a powerful tool for monitoring the nucleation and growth of C-S-H as they are independent of long range order. Furthermore, Raman or IR (ATR) spectra can be obtained within seconds. Yue et al. 2020 [15] demonstrated the potential of

* Corresponding author.
E-mail addresses: angela.ullrich@kit.edu (A. Ullrich), krassimir.garbev@kit.edu (K. Garbev), peter.stemmermann@kit.edu (P. Stemmermann).

https://doi.org/10.1016/j.cemconres.2026.108185
Received 16 December 2025; Received in revised form 16 February 2026; Accepted 17 February 2026
Available online 21 February 2026

Raman spectroscopy as they traced C-S-H, AFt, and AFm during clinker and cement hydration by optical fiber excitation Raman spectroscopy. Even a quantitative approach was applied in order to determine the carbonation of cement paste [16], although several drawbacks like possible drying and accelerated carbonation (change of the phase composition) as the laser beam is focused on a small sample volume seem inevitable. In addition, the limited probing depth (up to several micrometers) and orientation effects due to the polarized nature of the laser beam strongly influence the relative band intensities, leading to uncertainties in the quantitative approaches.

ATR spectroscopy is particularly sensitive to different H_2O environments and allows quick estimation of the consumption of the "free", unbound water present at the beginning of the hydration, and its incorporation into the hydrated phases with the progress of the hydration process. The method has also proved as a reliable method for *in situ* investigations [17] and quantification based on multivariate calibration [18,19]. First approaches to quantitative evaluation of *in situ* ATR data are based on the variation of peak heights and areas. However, the intensity of bands depends strongly on the contact pressure, and without the knowledge of the extinction coefficients of bands, the analysis is only semi-quantitative. For example, Ylmèn et al. 2014 [17] proved the consistency of peak heights determined *in situ and ex situ* on freeze-dried samples. In addition, they demonstrated agreement between the rates of change in vibrational bands and heat flow curves. Data evaluation is based on a complex data processing method, including subtraction of an initial spectrum and the water spectrum. A similar approach was pursued by Higl et al. 2021 [20]. They analyzed C-S-H formation as the variation of peak areas and compared the data to ^{29}Si-MAS-NMR by Pustovgar et al. [21]. Their peak fitting strategy includes subtraction of the water signal, linear background correction, creation of difference spectra by subtraction of the initial spectrum, and the final fit of Gaussian peak shapes with fixed FWHM. Another study by John et al. 2021 [22] focuses on the assignment of the different Si—O modes during hydration to silicate units based on ^{29}Si-MAS-NMR. However, both investigations were conducted on model systems, like pure alite or a mixture of portlandite and colloidal nano-silica suspension. Extension to the much more complex cement system should include at least the main phases in dry cement, C_3S (alite, Ca_3SiO_5), C_2S (belite, Ca_2SiO_4), C_3A (aluminate, $Ca_3Al_2O_6$) and C_4AF (ferrite, $Ca_2(Al,Fe)O_5$), and the hydration products C-S-H, CH (portlandite, $Ca(OH)_2$), AFt and AFm phases (Al_2O_3-Fe_2O_3-tri- or mono-substituted phases, $C_6AX_3H_n$ or C_4AXH_n with $X = OH^-$, SO_4^{2-}, CO_3^{2-}) [23]. Furthermore, in most studies, peak assignment is based on Q^0, $Q,^1$ and Q^2 silicate units obtained by NMR, although the peaks in the IR spectra should be described in terms of vibrations of bonds between individual atoms. In a recent publication, Garbev et al. 2025 [24] not only critically review the existing publications on this topic, but also provide an overall guide for the assignment of Si—O vibrational modes in the IR spectra of C-S-H phases in cement systems. Their assignment is validated by NMR spectroscopy as well as single-crystal polarized IR and Raman spectra of crystalline C-S-H phases and it serves as a solid base for the correct interpretation of *in situ* IR spectra of cement hydration.

This study focuses on early hydration and setting mechanisms of CEM I 52.5R (CEM I). The combination of *in situ* ATR-FTIR spectroscopy with *ex situ* and *in situ* XRD enables a comparative analysis of the reaction progress of clinker minerals and the formation of hydrate phases. Particular attention is given to the discussion of quantitative, semi quantitative, and structural information that can be drawn from the different analytical methods and evaluation techniques. Double experiments with three different water/cement-ratios (w/c-ratio) were conducted to check the reproducibility and plausibility of the results.

2. Material and methods

2.1. CEM I

CEM I 52.5 R of Holcim GmbH (Germany) was used in the experiments. For the hydration experiments, 5 g of the cement sample was mixed with water in water/cement-ratios (w/c) of 0.3, 0.37, and 0.45.

2.2. BET

Specific surface area of the CEM I was measured using a Quantachrome Nova 4000e (Quantachrome Instruments, Boynton Beach, FL, USA) with Nitrogen as probe and liquid nitrogen as coolant. All samples were dried under vacuum at 105 °C prior to analysis. Subsequently, fitting was performed according to the BET theory [25].

2.3. Thermal analysis (TA)

TA was performed in a Jupiter STA449 (NETZSCH, Selb, Germany). Samples were heated in Al_2O_3 crucibles (approximately 30 mg sample amount) with a heating rate of 10 K/min to temperatures of 1000 °C in N_2-flux, and the weight loss was determined.

2.4. X-ray fluorescence (XRF)

Chemical analysis of the CEM I was performed according to DIN 51729–10 by XRF analysis (Bruker AXS S8 Tiger). Repeated determination in two beads with different dilution factors (200 and 400 mg with 6 g Li-borate salt mixture) and certified cement standards are used for quality control. Before preparing the beads loss of ignition (LoI) was determined according to DIN 196–2 (30 min; 950 °C).

2.5. X-ray diffraction (XRD)

For XRD measurements, 5 g of the respective sample was mixed with water in a w/c-ratio of 0.37. The mixture was compacted in a 27 mm sample holder and covered with Kapton® foil to prevent dehydration and carbonation. Samples were measured with an Empyrean diffractometer (Malvern-PANalytical, Almelo, Netherlands) equipped with a multistrip PIXcel^{3D} detector (255 channels, simultaneously covering 3.347° 2θ), CuK_α-radition, and Bragg-Brentano-HD optics. Measurements were conducted in the range of 5° to 120° 2θ with fixed divergent and antiscattering slits of 0.25° and 1°, respectively, mask 10 mm, Soller slits of 0.04 rad (2.3°), and sample spinning (1 r/min). K_β-radiation was eliminated by Bragg-Brentano HD optics. Measurements were conducted every 15 min.

Phase identification was performed with the software packages Highscore-Plus *V*. 5 (PANalytical) and Diffrac-Plus (Bruker-AXS, Karlsruhe, Germany) using PDF 2004 (ICDD) and COD 2023 databases. Bulk quantitative phase analysis was performed with corundum as an external standard (α-Al_2O_3, Merck). In addition, measurements with 20% internal corundum standard were performed on dry CEM I and on the sample after the hydration experiment (divergent and antiscattering slits of 0.125°, and 0.5°, respectively). Refinements were performed with the Rietveld method following the fundamental parameters approach implemented in TOPAS V7 (Bruker-AXS) to determine crystalline and amorphous contents. The structure models obtained from the ICSD database and the additional parameters used for the Rietveld refinement are summarized in supplementary SI 1. The background was fitted with a 4th order Chebychev polynomial and 1/X Bkg, zero error, sample displacement, and absorption were refined. The size of the coherent scattering domains was determined by the double *V*oigt approach implemented in TOPAS 7.

The K-factor was calculated for corundum as an external standard according to:

$$K = \frac{S \bullet d \bullet V^2 \bullet MAC}{c}$$

where S is the scaling factor that is determined in the Rietveld refinement of the measurement of Al_2O_3. The variable *d* denotes the density, V the unit cell volume, MAC the mass absorption coefficient, and c is the concentration of the standard in the sample, hence for the pure corundum standard 100 wt%. The MAC of the corundum standard is 31.59 cm^2/g and the density 3.984 g/cm^3. The calculated K-factor was applied in the TOPAS software together with the MAC of the sample (64.31 cm^2/g).

2.6. ATR-IR spectroscopy (ATR)

The measurements were performed on a Tensor II spectrometer (Bruker Optics, Ettlingen, Germany) with a deuterated triglycine sulfate (DTGS) detector and a Golden Gate ATR cell with diamond crystal (Specac LTD, Orpington, UK). A specially developed sample holder for *in situ* hydration measurements was used (supplementary SI 2). The sample slurry was compressed with a contact pressure of 100 cNm on the diamond crystal. Three different water to cement ratios (w/c = 0.3, 0.37, 0.45) were investigated, with duplicate experiments performed with each w/c-ratio. Spectra with 64 scans were acquired every 2 min in the range 400–4000 cm^{-1} with a spectral resolution of 2 cm^{-1}. In contrast to XRD measurements, these spectra are not obtained on the sample surface, but at the bottom, and hence, portlandite formation due to surface water enrichment is avoided. The evaluation of the spectra obtained was performed by OPUS 8 software (Bruker Optics). The development of certain phases was evaluated by integration of their corresponding main bands in the spectra. In addition, peak fits were conducted on individual spectra using ORIGIN Pro 2023.

2.7. Calorimetry

A TAM Air calorimeter with 8 channels was used to measure the heat flow during hydration (Waters/TA Instruments, New Castle, US). Admix glass ampoules were filled with 1 g sample powder. Water was added by two syringes, each filled with 0.5 g H_2O. Measurement was conducted without stirring and at 25 °C.

3. Results and discussion

3.1. Phase evolution by XRD

3.1.1. Ex situ quantitative analysis of raw sample and hydration product

The raw sample of the dry CEM I was analyzed by BET, TA, XRF, and XRD with an internal standard in order to determine the specific surface, oxide, and phase composition (Table 1).

The BET surface area of 1.25 m^2/g is consistent with literature data on CEM I 52.5R (1.22 m^2/g, [26]). The CO_2 content determined by thermal analysis is 0.58 wt%, which corresponds to a $CaCO_3$ content of 1.32 wt%. This is higher than the value determined by XRD and indicates a minor presence of amorphous carbonate. The H_2O content is also below 1 wt%, and the sum of CO_2 and H_2O determined by TA is consistent with the LoI within ±0.1 wt%.

Regarding the chemical composition, CaO and SiO_2 account for 84 wt% of the sample with a C/S-ratio of 3.4. QXRD confirms the presence of high amounts of C_3S (56 wt%) and smaller amounts of C_2S (14 wt%) besides the minor clinker phases C_3A (8 wt%) and C_3AF (4 wt%). In addition to the Ca-sulfate phases, anhydrite and basanite, a minor quantity of CH (1 wt%), and traces of calcite appear as alteration products of the free lime (0.4 wt%). Alkali contents are below 1 wt%, and a minor amount of MgO appears in the form of periclase. The content of X-ray amorphous, and hence undefined material, ranges below 5 wt%.

The sample paste was hydrated in a glove box in N_2 atmosphere for 13 days. The water content was determined by TA (11.2 wt%). For comparison, phase contents of the hydrated sample were normalized to the dry sample amount. The amorphous content is much higher in the hydrated sample than in the dry raw sample, as low-crystalline phases like C-S-H and X-ray amorphous hydroxides or carbonates form during hydration. The amount in C_3S decreases by 66% and C_2S content decreases by 47%. The decrease in C_2S is almost exclusively observed in the low-crystalline and more reactive α'_H-C_2S phase. Whereas the coherently scattering domain size of β-C_2S is 121 nm, that of α'_H-C_2S ranges below 50 nm. High content of crystalline ettringite (AFt) was observed in the hydrated CEM sample due to the consumption of C_3A and C_3AF and the sulfates, anhydrite and bassanite. The high C/S ratio results in portlandite contents exceeding 10 wt%.

Table 1
Results from BET, TA, XRF, and XRD analyses of the dry CEM I and the sample hydrated for 13 days (w/c = 0.37). XRD results of the hydrated sample were normalized to the dry CEM I content. CO_2 and H_2O were calculated as weight loss 29–500 and 500–900 °C, respectively (an error of 0.1 wt% is estimated from the overlap of H_2O and CO_2 release in the range 400–500 °C). Phase contents were determined quantitatively (additional phase contents ≤1 wt%: hemicarbonate, arcanite, periclase, wollastonite). Estimated standard deviations (e.s.d.) of the Rietveld refinements are given in brackets.

	CEM I 52.5R	
Surface area (m^2/g)	1.249	
TA (wt%)		
H_2O	0.52	
CO_2	0.58	
LoI (wt%)	1.16	
RFA (wt%)		
CaO	64.08	
SiO_2	20.02	
SO_3	3.85	
Al_2O_3	5.11	
Fe_2O_3	2.03	
K_2O	0.67	
Na_2O	0.34	
MgO	1.2	
TiO_2	0.29	
XRD (wt%)	**Raw sample**	**Hydrated 13 days**
amorphous	4(1)	57.9(8)
C_3S	56(1)	18.8(8)
β-C_2S	8.3(4)	6.9(3)
α'_H-C_2S	5.8(4)	0.6(1)
C_3A	8.2(4)	4.1(4)
C_2AF	4.1(2)	2.1(1)
ettringite (AFt)	–	7.3(2)
portlandite	1.3(2)	11.7(1)
anhydrite	7.5(1)	0.8(1)
bassanite	2.1(1)	0.10(7)
gypsum	–	0.9(2)
calcite	0.3(2)	–
lime	0.36(8)	–
sum	98(4)	111(2)

3.1.2. In situ quantitative phase evolution during hydration

Fig. 1 depicts the variation in main phases with time, determined by *in-situ* X-ray diffraction during the first two days of hydration. Data was evaluated every 15 min within the first three hours, then the refinements were reduced to 30 min intervals and after eight hours to intervals of 1–3 h (supplementary SI 3). Comparably low water content (w/z = 0.37) was chosen for the experiments as water enrichment on the sample surface is expected. For comparison, all phase contents are normalized to the content of the dry binder. Immediate decrease in C_3S content after water addition is followed by a dormant period of 2.5 h (Fig. 1A). Afterwards, C_3S is consumed continuously within 20 h of hydration. This correlates with the range of portlandite formation. Correlation with C-S-H formation can be assumed although the low-crystalline phase can not be directly determined from XRD measurement. The content in crystalline C_2S (sum of α'_H- and β-C_2S) ranges around 7 wt% by addition of

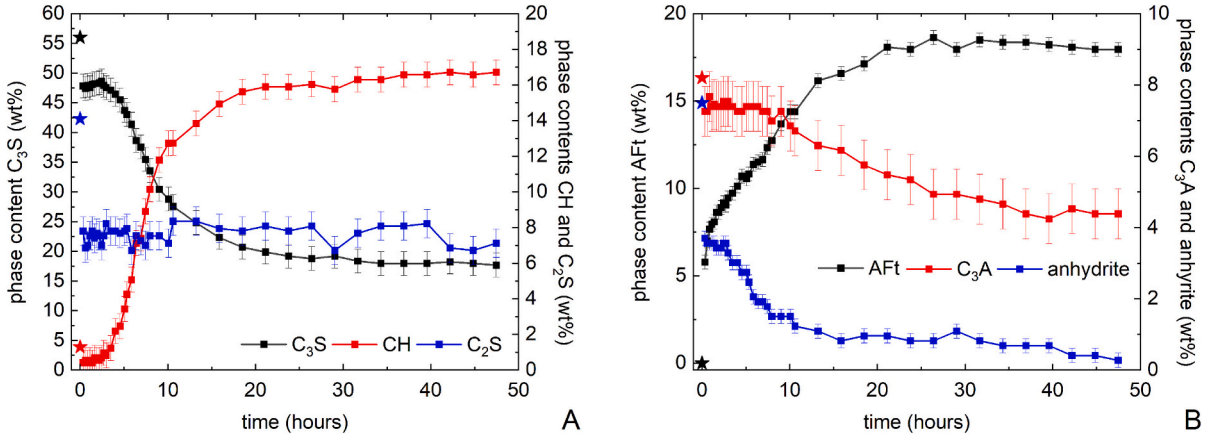

Fig. 1. *In situ* X-ray diffraction of C_3S, CH, and sum of α'_H- and β-C_2S (A) and AFt, C_3A, and anhydrite (B). Evolution of main phases with time. Data points of dry CEM I are indicated by stars. Estimated standard deviations of respective phases in Rietveld refinements are given with vertical bars.

water. As expected from the measurements with internal standard, no further change is observed after the immediate consumption of low-crystalline α'_H-C_2S. C_3A contents range around 7.3 wt%, and no significant reduction is visible before 10 h of hydration (Fig. 1B). The decrease afterwards is less steep compared to C_3S and corresponds to the slope of AFt formation. But in contrast to the constant C_3A values within the first hours, a very steep increase in AFt content is observed after water addition, and the beginning can only be estimated from the measurement of the dry sample and the first data points collected. In the very beginning, the decline in C_3A mirroring AFt growth could be obscured by the comparably large absolute errors determined for the C_3A contents. However, according to the formula of ettringite, only 0.6 wt% Al_2O_3, besides 1.3 wt% SO_3, are required for the formation of 7 wt% AFt. Hence, the reductions of about 1 wt% in C_3A and 4 wt% in Ca-sulfates, respectively, due to initial dissolution within the first 20 min, provide sufficient Al_2O_3 and SO_3 for immediate AFt formation.

Comparison of the absolute values with those determined with internal standard after 13 days confirms the contents of C_3S, C_2S, and C_3A as residuals of the original cement (±1 wt%). Anhydrite is almost consumed after the first 11 h of hydration (Fig. 1B). This underlines the reasonability of the quantification with external standard method. Nevertheless, the amounts of ettringite and portlandite calculated are far too high in the *in-situ* experiments (17.7 and 16.4 wt%) compared to those for the re-prepared samples afterwards (7.3 and 11.7 wt%). This shows the limits of *in-situ* X-ray diffraction in the context of hydration experiments. On the one hand, XRD data is collected in reflection on the top side of the sample, where H_2O tends to accumulate due to "bleeding" as the solid components settle down. Such solutions on the surface of the sample and beneath the Kapton foil quickly become oversaturated, promoting the augmented formation of particular phases like portlandite and ettringite instead of C-S-H in the measured sample area. On the other hand, the binding phase C-S-H that forms during hydration can only be obtained as included in the X-ray amorphous material, which also contains other components like H_2O, and low-crystalline calcite or portlandite. In addition, due to the duration of preparation and measurement, the first dataset is obtained after 19 min, where the formation of ettringite is already very advanced.

3.2. Phase evolution by ATR FTIR spectroscopy

3.2.1. ATR spectra of clinker and hydrated phases

Fig. 2 depicts the spectra of the original cement and the sample hydrated for one day. Slight carbonation is evident in both spectra as a weak and broad band centered around 1420 cm^{-1}, which is assigned to the ν_3 antisymmetric C—O stretching mode [27]. The weaker ν_2 CO_3 out-of-plane deformation mode and the ν_4 OCO bending modes of CO_3^{2-} expected below 900 cm^{-1}, are masked by the peaks of clinker phases. Pure samples of C_3S, C_2S, C_3A, anhydrite, AFm, AFt, C-S-H, H_2O, and CH were measured for comparison, and the peak positions of the strongest modes are marked according to the literature given.

The dry cement sample shows main absorption bands in the range 800–1000 cm^{-1}, which are characteristic for the strong ν_3 antisymmetric Si—O stretching vibrations in C_3S and C_2S [28,29], whereas the ν_4 antisymmetric bending modes are expected to appear below 600 cm^{-1}. Sharp ν_3 antisymmetric stretching bands of Al—O bonds in C_3A contribute to the frequency range between 700 and 900 cm^{-1} [30]. A clear assignment of the ferrite modes is not possible due to their low quantity and the strong peak overlap of the broad ferrite and sharp C_3A modes with the modes of the main clinker phases C_3S and C_2S. Due to the absence of well resolved peaks, this phase will not be included in the evaluation. By comparison to the measurement of pure anhydrite, the broad asymmetric peak centered between 1094 and 1120 cm^{-1} is ascribed to antisymmetrical stretching modes of sulphate anion (ν_3-SO_4^{2-}) [31,32]. The weaker antisymmetric bending vibrations appear below 700 cm^{-1} (ν_4-SO_4^{2-}). Strong S—O antisymmetric stretching vibration is also seen in the spectra of the hydrate sample assigned to AFt [32,33]. The corresponding peak could be differentiated from the analogous peak of anhydrite by its sharp and symmetrical shape. In addition, water absorption bands appear between 1600 and 1700 cm^{-1} (ν_2 H_2O), at 3420 cm^{-1} (ν_1), and at 3635 cm^{-1} (ν OH_{free}). Al-O-H bending vibrations are located at 855 cm^{-1}, whereas Al—O stretching vibrations give rise to bands below 600 cm^{-1}.

With progressive hydration, the initially formed AFt is expected to be replaced by AFm [33]. Therewith, the asymmetric stretching mode would be centered at a lower wavenumber, and the singlet in AFt broadens to a doublet in AFm. The bending vibration of excess water appears between 1600 and 1700 cm^{-1}, and the broad band centered around 3400 cm^{-1} in the high wavenumber region is due to symmetric and antisymmetric O—H stretching modes of H_2O. The strong bands of excess H_2O superimpose the OH bands of AFm and AFt and C-S-H in the high wavenumber region of the spectrum of hydrated CEM. The dominant feature in this region of hydrated CEM is the sharp band at 3645 cm^{-1} assigned to the O—H stretching mode of portlandite [32].

The Si—O modes of C-S-H appear in the spectrum of the hydrated sample as broad bands centered between 650 and 1050 cm^{-1}. A detailed analysis of the vibrational modes in C-S-H, not only in terms of silicate polymerization but also by resolving the contributions of specific silicon (paired, bridging) and oxygen (bridging, non-bridging) atoms, was conducted in a previous study by Garbev et al. 2025 [24]. A brief summary of the findings and the peak assignment elaborated in this publication will be given in this chapter. As the C-S-H shown in Fig. 2 has a C/S-ratio of 1, it contains Q^1 and Q^2 silicate units. The structure lacks a

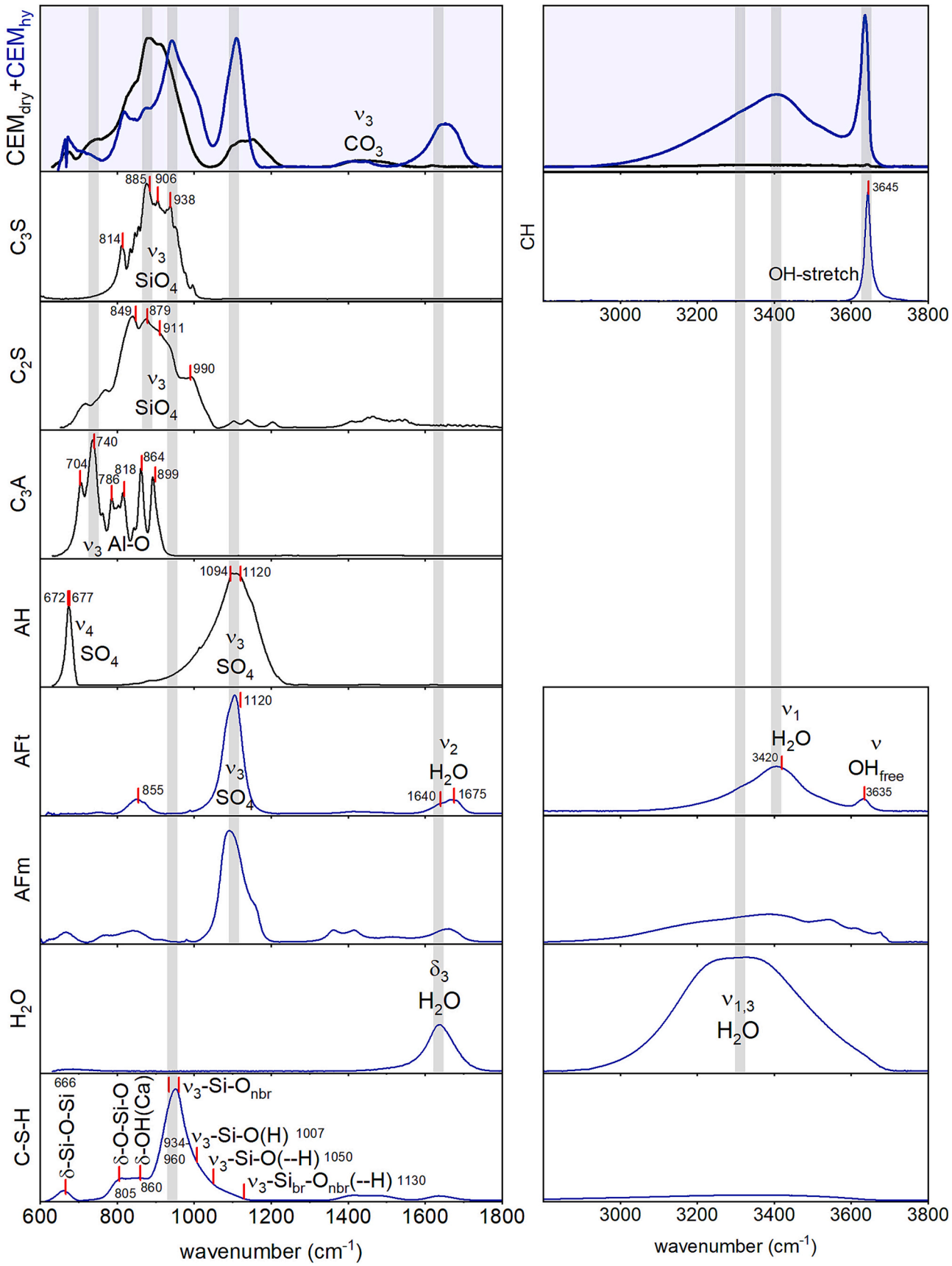

Fig. 2. Overview of ATR spectra of original cement and hydrated samples of CEM I 52.5R divided into low wavenumber region (left) and water region (right). AH = anhydrite, C-S-H with C/S = 1. Spectra of pure substances were measured for comparison: anhydrite (AH, Merck, p.a.), portlandite (Merck, p.a.), synthetic pure clinker phases (C_3S, C_2S, C_3A [34]), AFt and AFm (courtesy H. Pöllmann), synthetic C-S-H with C/S = 1 [35].

long-range order; therefore, it is possible to obtain bands for symmetric and antisymmetric modes. The band at 666 cm^{-1} was ascribed to δ-Si-O-Si vibrations with some stretching involved. The band at 805 cm^{-1} is distinctly visible in Ca-rich C-S-H, and according to a similar mode in jaffeite, it was described as "rattling" of Si within the "oxygen cage", which means that all seven oxygens in a Q^1 unit move against the two silicate atoms within the channels embedding the Si_2O_7 group (δ-O-Si-O). This movement also involves ν_3 Si-O_{br} vibrations. The low-intensity band at 860 cm^{-1} only appears in Ca-rich C-S-H and corresponds to the libration of OH groups bonded to Ca (δ-OH(Ca)). Based on the fact that the number of Si-O_{nbr} is higher than Si-O_{br}, the strong mode at 900–1000 cm^{-1} could be divided into contributions of Si-O_{nbr} of Q^1 dimers (934 cm^{-1}) and contributions of Si-O_{nbr} of Q^2 chain structures (960 cm^{-1}). In general, a high degree of silicate polymerization is correlated to a higher frequency vibration. However, the contributions of the individual Si-O bonds should also be taken into account. Here, it has to be distinguished between structures with exact saturation of bridging atoms (Si-O-Si angle = 180°) where the Si-O_{br} antisymmetric stretching modes appear at higher frequencies than those of Si-O_{nbr}, and structures with overbonded O_{br}, like C-S-H (Si-O-Si angle~138°). Overbonding of O_{br} results in underbonding of O_{nbr} and hence shorter bond lengths and higher frequency vibrations for Si-O_{nbr}. This is evidenced, for example, in the spectrum of the chain silicate 14 Å tobermorite, where stretching modes of Si-O_{nbr} are observed at higher frequencies than Si-O_{br}. Consequently, the contribution of ν_3 Si-O_{br} is observed in low-Ca C-S-H as a shoulder at 920 cm^{-1}. In addition, it has to be noted that also the incorporation of Al (electronegativity = 1.6) instead of Si (electronegativity = 1.9) can cause an elongation of bond length and hence a shift to lower frequency of the main Si-O_{nbr} band. However, increased polymerization could reverse this trend [36]. In addition, the presence of Si-OH environments further complicates the assignment as they appear generally at higher wavenumbers. This becomes particularly important at low C/S, where polymerization and the number of Ca-vacancies increase, and silanol environments are required to maintain charge balance. Therefore, the mode at 1007 cm^{-1} is ascribed to silanol groups (ν_3 Si-O(H)) with contribution of ν_3 Si-O_{nbr} from the bridging tetrahedra. On the one hand, Si-O(H) bond lengths are expected to decrease with increasing polymerization and therewith could give rise to higher frequency vibrations. On the other hand, the involvement of silanol groups in H-bonds also shifts the vibrational frequencies to higher wavenumbers. Hence, the high frequency bands at 1050 and 1130 cm^{-1} were ascribed to the OH-H_2O interactions ν_3-Si-O(−-H) and ν_3-Si_{br}-O_{nbr}(−-H), respectively. Although a clear separation of the modes is only partially possible, the publication of Garbev et al. [24] provides the fundamental basics for the assignment of the main C-S-H vibrational modes that are applied in the current publication.

3.2.2. *In situ investigation of qualitative phase variations by integral area fits*

Integral area fits within selected ranges of the ATR spectra (Table 2) provide a fast tool to observe the water consumption and dissolution of cement components parallel to the nucleation of C-S-H and other hydration products. Measurement from the bottom of the sample also enables more reliable detection of a representative sample area compared to the measurement on the sample's surface (XRD). Fig. 3A depicts the evolution of integral peak area of the δ-H_2O mode (1550–1785 cm^{-1}), during hydration with different w/c-ratios. The general trend with the highest initial value for w/c-ratio of 0.45 and the lowest value for 0.3 is reasonable. In addition, the datasets illustrate the drop in the intensity of the H_2O bands, mostly between 2 and 10 h of hydration. This could be explained by the consumption of unbound H_2O upon formation of hydrate phases. In addition, this seems to take place earlier in the sample with the lowest H_2O, and as expected, the corresponding drop in the intensity is smaller.

Table 2
Wavenumber ranges used for calculating integral areas.

Mode	Wavenumber range (cm^{-1})
δ-H_2O	1550–1785
O-H stretching CH	3583–3668
ν_3-Si-O C-S-H	900–1050
ν_3-S-O AFt	1040–1180

However, there are significant differences between the datasets of repetitive measurements. Several reasons are conceivable for these deviations. First, although the contact pressure was adjusted to similar values in all measurements, local variations can occur due to rapid sample preparation. Second, local water enrichment or depletion can occur due to inhomogeneous mixing or hydration reactions. This could be improved by applying a standardized mixing procedure, for example by the use of a laboratory vibrating table. Though this would increase preparation time. As the initial values for δ-H_2O are equal in the two mixtures with w/c = 0.45 and differ in the mixtures with w/c < 0.4, improper mixing due to low w/c-ratio is assumed.

Fig. 3B, C, and D show the comparison of the variation of integral areas of δ-H_2O, the O—H stretching mode of CH (3583–3668 cm^{-1}), and the ν_3-Si-O stretching modes of C-S-H (900–1050 cm^{-1}) for the samples with w/c-ratios of 0.3, 0.37, and 0.45, respectively. Due to the overlap of the bands typical for the C_3S and C-S-H modes, negative values appear in the data of C-S-H within the first 4 h of hydration. They were set to zero, and all data was normalized to a maximum of 100% afterwards.

All diagrams show that the initial steep decrease in intensity of the δ-H_2O mode strongly correlates with the increase in peak area of the integration range for portlandite. In the latter stages, the decrease flattens, which correlates with the increased C-S-H formation. As the H_2O consumption displays the formation of hydrate phases, it can serve as a marker for cement setting. Again, the comparison between w/c = 0.45, 0.37, and 0.3 shows that higher H_2O contents lead to a delay in H_2O consumption and hence the formation of hydrates. C-S-H formation starts after around 5 h of hydration and follows the trend of steep increase in the sample with low w/c and slower growth at high w/c-ratio, which is also observed in water consumption and CH formation. Determination of integral peak areas provides a fast method to obtain reasonable results in terms of hydration kinetics. This is also demonstrated by comparison to calorimetric data. Fig. 3D shows consistency between the time frame of highest reaction rates and the heat flow maximum for the sample with a w/c-ratio of 0.45. However, the example of C-S-H integral area shows how peak overlap masks early-age evolution. Particularly in the range of S—O, Si—O, and Al—O asymmetric stretching vibrations below 1200 cm^{-1} (Fig. 2), massive peak overlap indicates the necessity to regard individual peaks rather than integral areas.

3.2.3. *Phase transitions and structural changes during hydration*

As a prerequisite for peak deconvolution, the spectra have to be analyzed in detail in order to define the required parameters as well as suitable constraints for the modes of individual phases. Ettringite precipitation is known to be the main process that drives the change in rheology during the first two hours of hydration before C-S-H formation and setting [37].

In a first approach, the variation in the ν_3-S-O asymmetrical stretching mode of AFt was calculated as a change in integral areas with hydration time (1040–1180 cm^{-1}, Fig. 4A).

A rapid increase of AFt within the first minutes of hydration is observed in all samples, independent of the water content. The integral areas rise immediately after water addition to maxima after 5, 6, and 7 h of hydration for the samples with w/c-ratios of 0.3, 0.37, and 0.45, respectively. This is followed by a slight drop, whereafter the sample with low water content shows further degression and the samples with higher w/c-ration show a marginal increase. It is expected that water depletion during hydration of clinker phases and the incorporation of sulfate and calcium in other phases leads to decomposition of AFt

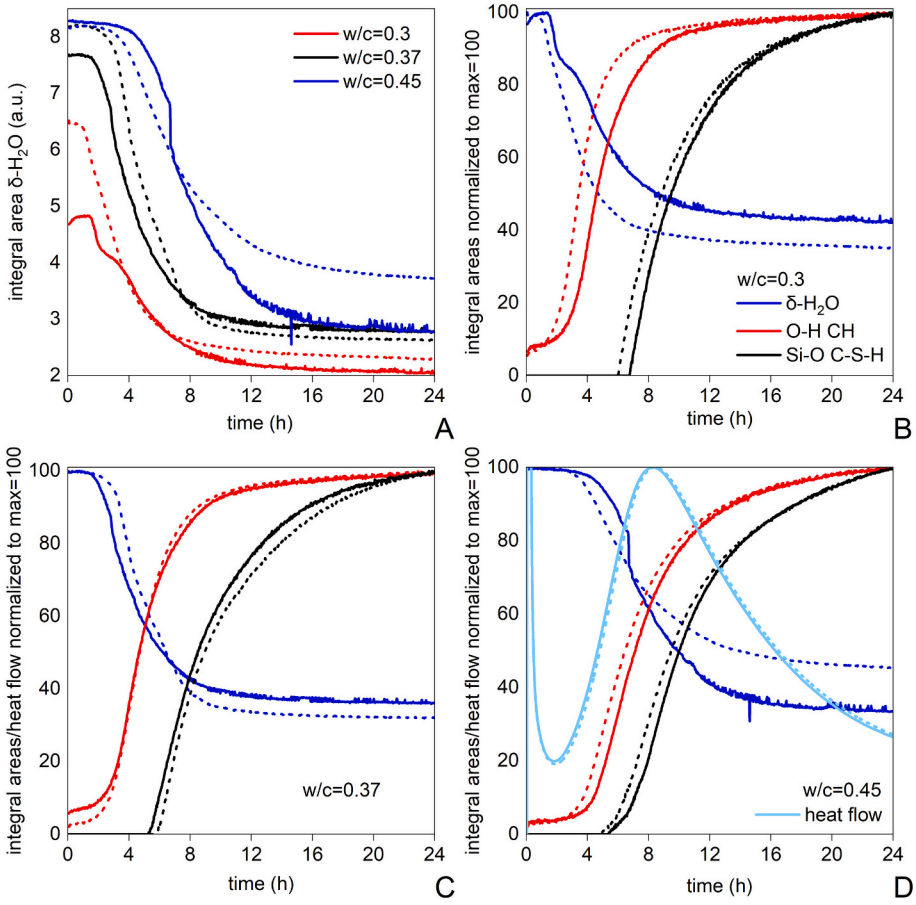

Fig. 3. Integral areas of δ-H_2O determined for samples with different w/c-ratios (A). Hydration experiments with w/c-ratio = 0.45 (B), w/c = 0.37 (C), and with w/c-ratio of 0.3 (D): Normalized integral areas for δ-H_2O, O—H portlandite, and ν_3-Si-O_{nbr} of C-S-H. The two datasets are indicated by continuous and dashed lines. Color scheme in C and D according to B. Calorimetric data obtained with w/c-ratio = 0.45 is shown for comparison.

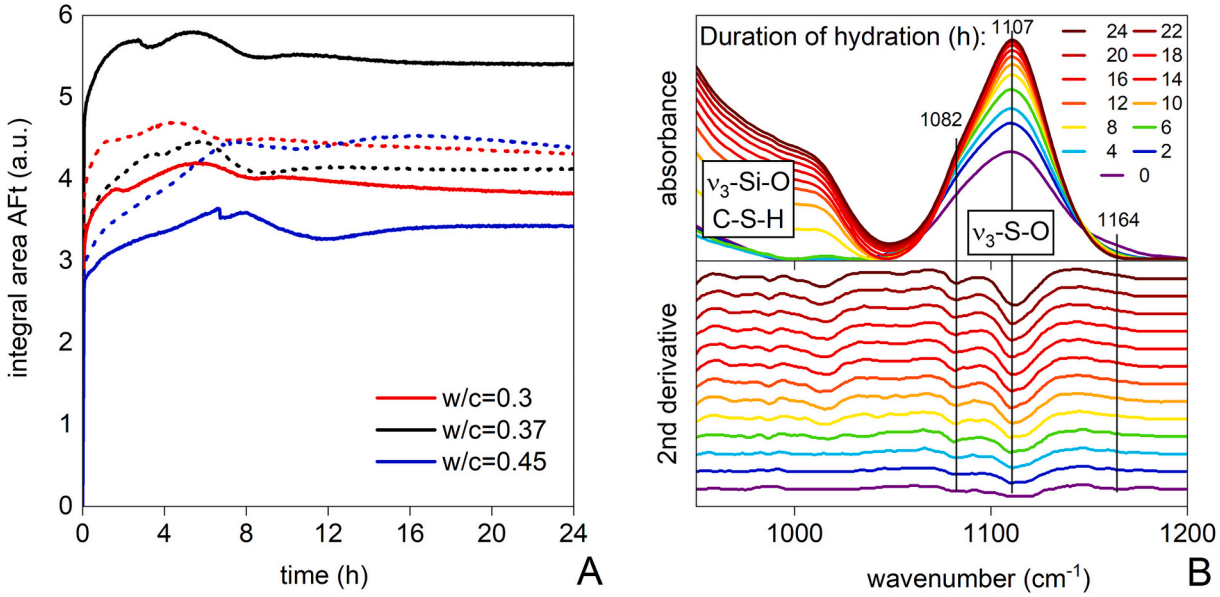

Fig. 4. Integral areas of ν_3-S-O determined for samples with different w/c-ratios (A). Detailed view of the variation of the ν_3-S-O peak and its second derivative during hydration for the sample with w/c = 0.45 (B).

($Ca_6Al_2(SO_4)_3(OH)_{12}{\cdot}26H_2O$) to monosulfate ($Ca_4Al_2SO_4(OH)_{12}{\cdot}6H_2O$) as observed also in heating experiments [38]. Possible transformation of AFt to AFm is checked for the sample with w/c = 0.45 by the variation of peak shape and second derivative of peaks (Fig. 4 B).

After 4 min of hydration, a distinct indication for residual anhydrite is visible, particularly in the high-wavenumber shoulder. However, as

already evidenced by XRD, the narrow peak form indicates that most sulfate occurs in the form of AFt With progressing hydration FWHM decreases and the peak increases in height, witnessing further growth and enlargement of the ettringite crystals. No systematic shift in peak position during hydration and no broadening towards higher wavenumbers is visible. On the contrary, at later hydration stages, a low wavenumber shoulder appears, which can also be seen in the spectrum of pure AFt (Fig. 2). This shoulder could also be enhanced due to the overlay with the strong and broad C-S-H modes centered around 1007 cm^{-1}. Hence, within the first 24 h of hydration, no indication is found for broadening of the narrow AFt mode to the characteristic doublet of AFm (1093 and 1145 cm^{-1}). Such observations show the limits of integral area determination where peak form and peak overlap are not accounted for. From the visual inspection of peaks, a continuous increase in the ν_3-S-O mode is expected, where only the growth rate slows down with time. But due to the overlay with residual anhydrite and C-S-H modes, and due to the narrowing peak form, this trend is not visible in Fig. 4A. In addition, the graph shows the variation in absolute values, which indeed describes the kinetics of formation and growth of ettringite, but lacks absolute quantitative information.

Fig. 5A depicts the evolution of main peak intensities for the clinker phases with hydration time for the sample with w/c-ratio = 0.45. Two peaks can be distinguished at early hydration stages, a strong band at 920 cm^{-1} and a weaker one centered at 880 cm^{-1}. However, comparison to the IR spectra of dry cement shows that the dominating Si—O stretching is at 880 cm^{-1}. It reflects the fact that the major phase in CEM I is C_3S (Fig. 2).

The strong band at 920 cm^{-1} is observed even in spectra taken a few minutes after the beginning of the hydration, *i.e.*, far before any formation of C-S-H takes place. On the other hand, the spectrum of pure H_2O does not possess any bands in this area. Therefore, the enhanced intensity at 920 cm^{-1} could be interpreted as a possible indication for interaction of H_2O with the clinker minerals. This could include the formation of Si-OH environments on the surfaces of C_3S within the first minutes after water addition.

The bands at 880 cm^{-1} and 920 cm^{-1} decrease within the first hours of hydration, and after 5 h, a band at 939 cm^{-1} appears, representing the Si—O asymmetric stretching vibrations in C-S-H. The first stages of dissolution of C_3S include decalcification and the formation of an electrical double layer around etched C_3S grains. Due to the high concentration of dissolved Ca^{2+}, the pH of the solution is extremely high at the beginning of the hydration, thus triggering the formation of Si-OH. The double layer, therefore, consists of Si-OH environments followed by a diffuse layer of H_2O and Ca^{2+}. As long as the pH remains quite high, the polymerization is restricted. H_2O stabilizes the environment around the OH groups by H-bonds [39]. The presence of surface Si-OH groups was confirmed on Si surfaces by the 3745 cm^{-1} band (free O—H vibration) and corresponding H-bonds with H_2O at 3525 cm^{-1} [39,40]. In our case, due to the presence of a huge quantity of free H_2O in this hydration stage, it is impossible to discern them in the high frequency part of the IR spectrum. Nevertheless, one can assume a change of the corresponding Si-O(H) vibration, which we assign to the band at 920 cm^{-1}. Several studies confirm such assignment of bands in the range 920–980 cm^{-1} in the IR and Raman spectra of silicates [41,42,43]. Partial polymerization on the inner surface of C_3S cannot be ruled out, which would lead to the formation of Si-O-Si silanes and, depending on the saturation rate, possibly to the formation of a Si-rich protective layer [44,1]. The occurrence of a band at 939 cm^{-1} on a later stage, points to the

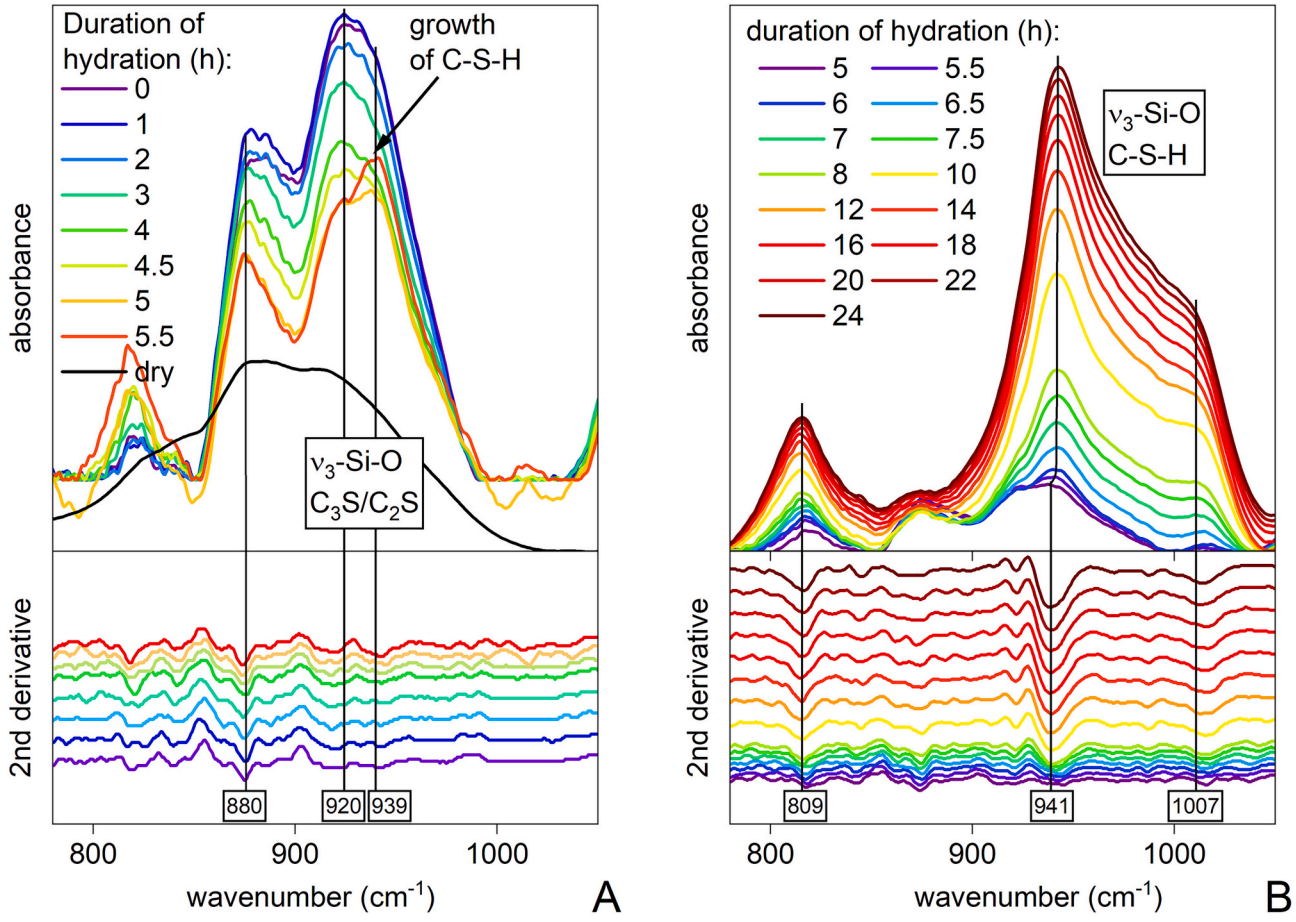

Fig. 5. Detailed view of the evolution of peak intensities and second derivative in ATR spectra with hydration time (w/c = 0.45). (A) Initial consumption of clinker phases (0–5,5 h) and (B) growth of C-S-H (5-24 h).

formation of Si-O-Si environments by oxolation [45]. Similar observations were made by Morrow and Devi [46] where formation of Si-O-Si upon depletion of Si-OH was postulated. An important prerequisite for this to happen is a change of the pH triggered by the formation of Ca$(OH)_2$, which serves as a surface for the nucleation of the C-S-H by heterocondensation [45]. Fig. 3 shows that the formation of $Ca(OH)_2$ always precedes that of C-S-H, which confirms that assumption. Therefore, we consider the sudden change of the band frequency from 920 to 939 cm^{-1} as a marker for C-S-H nucleation. Possible $(H_2O)(OH)_3Si\text{-}O\text{-}Si(OH)_3(H_2O)$ species may also exist in the solution after the start of the CH precipitation, but it is expected that, due to the longer Si—O bonds [47], their ν_3-Si-O frequency would be lower than that of Si_2O_7 species and thus undistinguishable from 920 cm^{-1}. Higher polymerized Si—O than Si_2O_7 is not expected on the time scale of hydration in this study [48].

Fig. 5B shows the progressing hydration after C-S-H nucleation. The peak at 939 cm^{-1} shifts to 941 cm^{-1} between 5 and 6.5 h of hydration. An increase in polymerization is unlikely in the period of early hydration, except for the theory of formation of a protective Si-rich layer by Kalousek et al. 1946 [44]. Such an increase in silicate polymerization is achieved *via* the appearance of bridging tetrahedra interconnecting the paired (dimeric) ones. Thus, an increased intensity on the low frequency side of the main envelope (920 cm^{-1}) is expected as suggested in [24]. Incorporation of Al in bridging sites should have a similar effect on the spectrum but would appear as a shoulder at a lower frequency (900–910 cm^{-1}, due to the longer Al—O bonds) [36]. As these are not apparent, we suggest that no increased polymerization by both Si and Al in bridging sites takes place within the time scale of the *in situ* experiments.

Therefore, we assume that the small shift towards higher frequency in the first hours of C-S-H formation is mostly due to an increase in the particle size up to the point where the growth is hampered by the confined space. The overall increase in the intensity and area of the 941 and 1007 cm^{-1} bands is due to increased formation of C-S-H. No shift is visible in the peaks after 6.5 h of hydration. The peak at 809 cm^{-1} is strongly overlain by peaks of residual clinker phases at the beginning of the hydration, but its intensity increases with time, once again confirming the enhanced formation of dimeric silicate species and the lack of Q^2 within the hydration time investigated. In addition, a contribution of OH libration (Ca-OH bending) from C-S-H is expected to appear at about 860 cm^{-1} as seen from the IR spectra of pure Ca-rich C-S-H phases (Fig. 2). But the overlap with the Al-O-H bending mode of ettringite has to be watched carefully in this range.

3.2.4. Peak deconvolution

In the first step, characteristic peaks for individual phases were determined from the spectra of pure phases shown in Fig. 2. In the second step, a peak fitting routine was developed in order to describe the increase in C-S-H and ettringite modes with minimal contribution of other phases and to display the parallel consumption of raw clinker phases. Selected datasets of the experiments conducted with w/c-ratio = 0.45 were fitted by peak files including all peaks and constraints described in the following.

Data processing starts with the subtraction of the spectrum of pure H_2O as described in [17] and [20]. A background correction (rubberband method, 1 iteration) was applied in the range 600–4000 cm^{-1} afterwards. For the following peak fits, only the data range between 800 and 1200 cm^{-1} is taken into account. Convergence to $Chi^2<1E^{-6}$ was reached in all fits. Peak deconvolutions for the data obtained after 5 min and 24 h are shown in Fig. 6.

Prior to peak fitting on the sample spectra, basic peak datasets for the individual phases were obtained from the measurements of pure substances starting from literature values (see chapter 3.2.1 for references). For C_2S and C_3A, these resulting peak positions, full widths of half maximum (FWHM), and peak area ratios were kept fixed in the refinements of the experimental data. For the main clinker phase C_3S, more variables are required to account for the change in peak ratio of the main Si—O stretching bands due to the formation of Si-OH bonds during early hydration, as discussed in 3.2.3. Hence, all peak parameters describing the vibrational modes of C_3S in the ν_3 Si—O region, and these fitting the band at 920 cm^{-1}, which increases significantly upon contact with water, were re-refined using the initial dataset at the onset of the hydration experiment. Peak positions, FWHM, and area ratios were then kept constant in all subsequent peak fitting procedures. The only exception was the ν_3 Si—O mode at 920 cm^{-1} for which an unconstrained refinement of the peak area was permitted up to 4 h of hydration, after which the formation of C-S-H commences. As discussed in 3.2.3, the modes of anhydrite are visible in the high wavenumber shoulder of ν_3-S-O AFt. In order to account for that, peak positions of anhydrite were re-refined on the first dataset, whereas the FWHMs and area ratios were kept constant according to the measurement of the pure anhydrite sample.

For the hydrate phase AFt, the peak area ratio between ν_3-SO_4 and the Al-O-H bending mode was refined on the measurement of pure ettringite. Position, area, and FWHM for ν_3-S-O were refined during all peak fits. Due to low intensity and strong peak overlay position, FWHM, and area ratio (ν_3/ν_4) were fixed for ν_4-S-O. Initial values for the C-S-H modes were refined on a reference material with C/S = 1.2. But as there is a strong dependency of the peak parameters on C/S-ratio [49], all parameters were re-refined on the measurement after 24 h. As the C-S-H structure lacks long-range order, all parameters should be refined independently. However, due to the strong overlap of C-S-H peaks and the overlay with clinker peaks, some constraints were applied. Table 3 summarizes the peaks and constraints for all phases. In addition, peak areas of clinker phases were constrained not to increase.

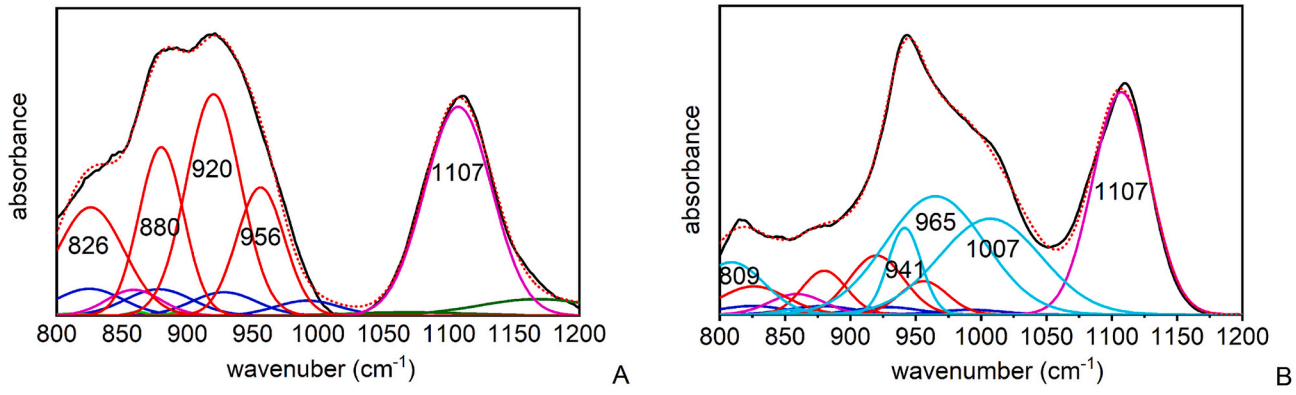

Fig. 6. Examples of peak fits to ATR data of the hydration experiments measured after 5 min (A) and 24 h (B). The measured data is depicted as black, and the fitted data as a dotted red line. The peaks of C_3S, C_2S, C_3A, AH, AFt, and C-S-H are shown in red, blue, green, olive, magenta, and cyan, respectively. (For interpretation of the references to color in this figure legend, the reader is referred to the web version of this article.)

Table 3
Peak data and constraints for the fits of ATR spectra on hydrated cement samples. *constraint applied after 4 h of hydration. **constraints applied between 5 and 8 h of hydration. Peak data for C_2S and C_3A was obtained from reference spectra (chapter 3.2.1), all other datasets were re-refined on the measured data.

Mineral	Peak position (cm^{-1})	FWHM (cm^{-1})	Area constraints	Possible assignment	Silicate species
C_2S	825	60	a	ν_s Si-O	Q_0
	878	60	=a·0.983	ν_{as} Si-O	Q_0
	928	58	=a·0.843	ν_{as} Si-O	Q_0
	992	57	=a·0.530	ν_{as} Si-O	Q_0
C_3A	813	25	b	ν_s Al-O	–
	862	17	=b·1.221	ν_{as} O-Al-O-	–
	895	22	=b·1.403	ν_{as} Al-O-Al/Al-O-	–
C_3S	826	60	h	ν_s Si-O	Q_0
	880	40	=h·1.037	ν_{as} Si-O	Q_0
	920	49	=h·1.712*	ν_{as} Si-O	Q_0
	956	43	=h·0.848	ν_{as} Si-O	Q_0
AH	1070	107	=c·0.202	ν_{as} S-O	–
	1168	107	c	ν_{as} S-O	–
AFt	859	49	=d·0.1	Al-O-H bending	–
	1109–1106	55–65	d	ν_{as} S-O	–
C-S-H	809	42**	=e·0.182**	δ-O-Si-O (+ν_3-SiO_{br})	Q_1
	857	67	–	δ-OH(Ca)	–
	934–947	22**	–	ν_3-Si-O_{nbr}	Q_1
	947–965	87**	e	ν_3-Si-O_{nbr}	$Q_1(Q_2)$
	1007	72**	–	ν_3-Si-O(H)/ν_3-Si-O(−-H)/ ν_3-Si_{br}-O_{nbr}(−-H)	

Full datasets of peak fits are given in supplementary SI 4. Peak areas of C_2S and C_3A are small compared to those of C_3S, and due to the strong overlap, clear separation is not possible. In Fig. 7A two selected peak areas of the main clinker phase C_3S are shown as a representative of clinker consumption and hydration of C_3S. Both peak areas decrease up to 12 h of hydration and remain constant afterwards. The area of the peak centered at 920 cm^{-1} is significantly larger than that of the peak at 880 $cm^{-1,}$ which is in accordance with the discussion in chapter 3.2.3. A steep increase in peak area at 920 cm^{-1} is observed from the first datapoints. This indicates that the formation of Si-OH takes place at the very beginning, immediately after water addition. After the first minutes of hydration, the mode centered at 920 cm^{-1} decreases similarly to all other ν_3 Si—O modes of C_3S.

For the C-S-H phase, selected peak areas and FWHMs are shown in Fig. 7B and C. As the peak area of the weak δ-OH(Ca) mode at 857 cm^{-1} varies below 0.12, it is not distinguishable from overlying peaks of clinker phases and AFt, and hence it will not be discussed. According to Fig. 5B and the discussion in 3.2.3, most peak positions were kept constant during the refinement. Only for the sharp ν_3-Si-O_{nbr} mode that appears at 939 cm^{-1}, a shift to 941.4(1) cm^{-1} is observed between 5 and 6.5 h of hydration. The broad ν_3-Si-O_{nbr} mode centered at 962(2) cm^{-1} was also refined but shows no systematic variation in peak position. However, the increasing peak areas provide further insight into C-S-H growth (Fig. 7B). In consistency with integral area fits, C-S-H peaks develop after about 4–5 h of hydration. There is a steep increase in the strong and broad ν_3-Si-O_{nbr} mode centered at 962 cm^{-1}. As within the first 24 h, dimers are expected to be the dominant silica species. The mode at 962 cm^{-1} is ascribed to the nucleation and growth of Q_1 silicate units with high intrinsic disorder and hence multiple environments for the Si_2O_7 species. After a short delay, ν_3-Si-O modes centered at 1007 start to increase. These bands appear due to silanol groups and their interactions with OH-H_2O. The sharp ν_3-Si-O_{nbr} mode centered at 941 cm^{-1} increases slowly and almost parallel to the growth of δ-O-Si-O at 809 cm^{-1}, which is attributed to “rattling” of Si within the “oxygen cage” and which also includes a contribution of ν_3-SiO_{br}. These modes reflect the formation of a less disordered C-S-H structure.

All FWHMs show a slight increase during early formation of C-S-H but remain constant after 15 h of hydration, except the FWHM of the shoulder at 1007 cm^{-1} which increases continuously between 13 and 24 h of hydration (Fig. 7C). This reflects an increasing variation in silanol environments due to their involvment in various H-bonds. With increasing polymerization Ca-vacancies form and more silanol environments are required to maintain the charge balance.

Peak deconvolution of the sulfate modes (Fig. 7D-F) indicates a shift in ν_3-SO_4 of Ettringite from 1107.6(3) cm^{-1} (0−1*h*) to 1106.6 cm^{-1} within the first 4 h of hydration. Both, the error determined during initial hydration and the shift towards lower wavenumbers can be attributed to imperfect separation of anhydrite and AFt modes. Although the contribution of anhydrite is distinctly visible at low hydration stage (Fig. 6A) the strong peak overlap leads to partial fit of the weak anhydrite modes by the much stronger AFt mode and therewith the shift to lower wavenumbers while anhydrite is consumed. After the first hour of hydration, anhydrite modes are no longer visible and AFt peak position increases to 1107.5 cm^{-1} again. It has to be noted, that the shift in ν_{as} S—O of AFt is below the limit of spectral resolution of the FTIR instrument (2 cm^{-1}). However, the observed trends support the observation in FWHM. These also reflect a scatter within the first hour (61.9(8) cm^{-1}). Both, the decreasing FWHM and the peak position of asymmetric stretching mode of AFt prove that there is no replacement of AFt by AFm as this would lead to the shift of asymmetric stretching mode to lower wavenumber and the broadening of the singlet in AFt to a doublet in AFm. In contrast to the calculation of AFt formation as integral areas, peak areas increase during 24 h of hydration. As expected from visual inspection (Fig. 4B) and XRD (Fig. 1B) there are changes in growth rate but overall, the content in AFt increases. Hence, the peak fits provide better approximation of phase evolution than the integral areas. In addition, normalization based on XRD data could even enable semi-quantitative analysis of the growth and consumption of individual phases.

4. Conclusion and outlook

Phase development during the hydration of a CEM I sample was followed by *in situ* XRD and *in situ* ATR spectroscopy. In contrast to XRD, ATR spectroscopy provides the possibility for direct measurement of the low-crystalline hydration product C-S-H and in addition to observe the evolution of phases from the very beginning of the hydration reaction. ATR spectroscopy is also a valuable tool for understanding complex solid solutions such as C-S-H and AFt phase as a base for thermodynamic modelling.

The study focusses on the development of a peak fitting procedure for CEM I samples that exceeds simple integral area fitting. This method provides the possibility to differentiate between the contributions of individual phases. In addition, early formation of Si-OH bonds on the electrical double layer on the interface clinker phases/water was shown. The interaction of the clinker phases C_3S and C_2S with water immediately results in an enhancement of the intensity of the band at 920 cm^{-1}, which has been for the first time attributed to the formation of Si-OH bonds at the interface of the clinker phases and water. However, due to the complexity of these silica-water interactions, including solution and formation of different aqueous species, this topic requires further investigation. The structural evolution in C-S-H and AFt hydrate phases was depicted in the context of the overall progression of hydration, encompassing the concomitant dissolution and precipitation processes. Strong dependence between the H_2O consumption, formation of Ca$(OH)_2$ and triggering of the C-S-H formation was established. An increase in polymerization by both Si and Al in bridging sites was found to be unlikely within the time scale of the *in situ* experiments. Also the transformation of AFt to AFm phase within the first 24 h of hydration, which has been assumed from the low ratio between calcium-sulfates and C_3A, was excluded based on peak center and width development.

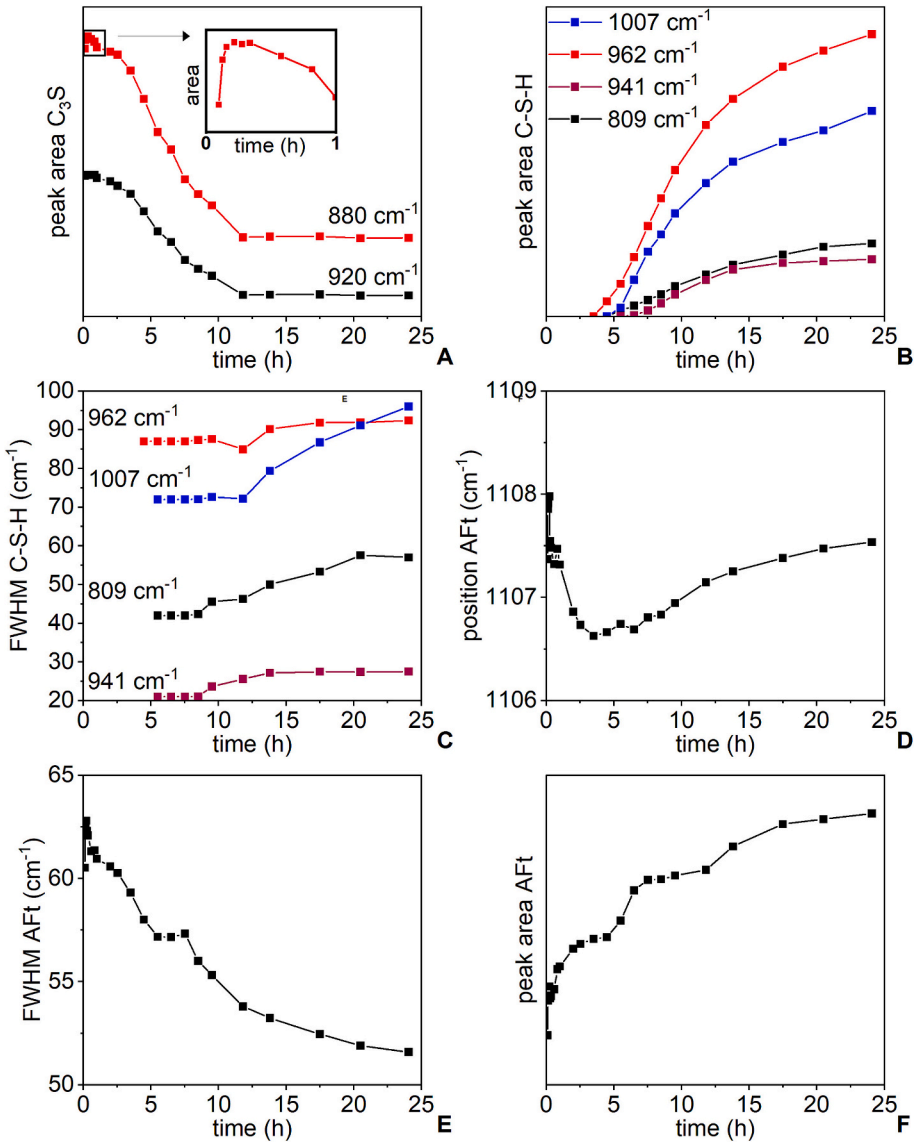

Fig. 7. Results from peak fits: selected peak areas of C_3S (A) and C-S-H (B) and selected FWHM of C-S-H peaks (C); peak position (D), FWHM (E), and peak area (F) of AFt.

It is expected in later hydration stages when the minor residual calcium-sulfates are consumed completely. In contrast to these more complex issues, there are other hydration processes that can be followed by simple integral area fits. Delay of hydration by increased w/c-ratio from 0.3 to 0.45 is evidenced by the drop of water signals and the formation of the hydrate phases, C-S-H, portlandite, and AFt. Hence, the peak analysis method has to be chosen according to the mode investigated and the parameters that are of interest. Whereas the evolution of the O—H stretching mode of portlandite or the variation of δ-H_2O can be obtained reliably from simple integral fits of the peak areas, strong overlap of silicate and sulfate modes requires more complex peak fitting strategies. Peak fitting provides the additional benefit of structural information.

However, as this is the first detailed analysis on the hydration of the multi-phase system of a cement paste, there are still limitations and challenges. One important issue is the reproducibility of ATR data. Mixing could be a problem in terms of w/c ratio, which may not be homogeneous. Fluctuations in sample density in the sample holder lead to different space available for crystal growth. Further work is needed on the reduction of such effects, for example, by a standard mixing procedure, reproducible filling of the sample holder, and by watching the contact pressure carefully. However, one must consider the time required for careful preparation relative to the brief interval before early-age strength-forming phases develop. In addition, there is still room for improvement in peak deconvolution, for example by extending the fit area. Nevertheless, the overlay of peaks from different phases hampers clear separation, particularly for phases that occur in low amount. In addition, structural changes within individual phases during hydration require further investigation to optimize the parameters and constraints for the fits. In particular, the changes in structure and particle size of low-crystalline C-S-H in cement paste require further investigation, for example by including validation of the findings by other methods like NMR spectroscopy.

CRediT authorship contribution statement

Angela Ullrich: Writing – review & editing, Writing – original draft, Methodology, Investigation, Formal analysis, Data curation, Conceptualization. **Krassimir Garbev:** Writing – review & editing, Writing – original draft, Methodology, Investigation, Formal analysis, Conceptualization. **Peter Stemmermann:** Writing – review & editing, Funding acquisition.

Funding

This research was funded by BMWK, grant number 03EE5130D (URBAN - Upcycling von Reststoffen aus der Betonaufbereitung, 01. november 2022–31. october 2025, https://enargus.de/pub/bscw.cgi/?op=enargus.eps2&q=%2201248895/1%22&v=10&id=10543324 and by DFG, grant number 541857967 (R-ClinkerControl: AI augmented control model for coping with fluctuating recycling waste in carbonate-melt clinkering for recycling-cement, since 2024, https://gepris-extern.dfg.de/gepris/projekt/541857967?language=en).

Declaration of competing interest

The authors declare that they have no known competing financial interests or personal relationships that could have appeared to influence the work reported in this paper.

Acknowledgements

We gratefully acknowledge Dr. Britta Bergfeldt, Julia Podszuweit, and Aaron Münch for the measurements and evaluation of XRF data. Additionally, we want to thank Günter Beuchle and Julia Podszuweit for the determination of BET specific surface area.

Appendix A. Supplementary data

Supplementary data to this article can be found online at https://doi.org/10.1016/j.cemconres.2026.108185.

Data availability

Data will be made available on request.

References

[1] E. John, B. Lothenbach, Cement hydration mechanisms through time – a review, J. Mater. Sci. 58 (2023) 9805–9833, https://doi.org/10.1007/s10853-023-08651-9.
[2] K.L. Scrivener, T. Matschei, F. Georget, P. Juilland, A. Kunhi Mohamed, Advances in hydration and thermodynamics of cementitious systems, Cem. Concr. Res. 174 (2023) 107332, https://doi.org/10.1016/j.cemconres.2023.107332.
[3] W. Zhang, L. CaO, X. Ren, J. Ye, L. Liu, Y. Wu, Influence of free calcium sulfate levels on the early hydration of sulfate-rich belite sulfoaluminate clinkers: a comparative study with anhydrite and gypsum, Cem. Concr. Res. 181 (2024) 107522, https://doi.org/10.1016/j.cemconres.2024.107522.
[4] E. Rubinaite, T. Dambrauskas, K. Baltakys, R. Siauciunas, Investigation on the hydration and strength properties of belite cement mortar containing industrial waste, J. Therm. Anal. Calorim. 148 (2023) 1481–1490, https://doi.org/10.1007/s10973-022-11556-5.
[5] Z. Yang, X. Tao, G. Wang, W. Li, Study on preparation of low heat high belite clinker from waste mortar and its modification, Materials 15 (2022) 3196, https://doi.org/10.3390/ma15093196.
[6] M. Borštnar, N. Daneu, S. Dolenec, Phase development and hydration kinetics of belite-calcium sulfoaluminate cement at different curing temperatures, Ceram. Int. 46 (2020) 29421–29428, https://doi.org/10.1016/j.ceramint.2020.05.029.
[7] M. Borštnar, C.L. Lengauer, S. Dolenec, Quantitative in situ X-ray diffraction analysis of early hydration of belite-calcium sulfoaluminate cement at various defined temperatures, Minerals 11 (2021) 297, https://doi.org/10.3390/min11030297.
[8] P.R. De Matos, J.S. Andrade Neto, D. Jansen, A. de la Torre, A.P. Kirchheim, C.E. M. Campos, In-situ laboratory X-ray diffraction applied to assess cement hydration, Cem. Concr. Res. 162 (2022) 106988, https://doi.org/10.1016/j.cemconres.2022.106988.
[9] B.H. O'Connor, M.D. Raven, Application of the Rietveld refinement procedure in assaying powdered mixtures, Powder Diffract. 3 (1) (1988) 1–6, https://doi.org/10.1017/S0885715600013026.
[10] A. Goncharov, S. Zhutovsky, Comparison of different approaches for quantification of amorphous phase in hydrated cement paste by XRD, in: RILEM Bookseries 43, Springer, 2023, pp. 449–459, https://doi.org/10.1007/978-3-031-33211-1_40.
[11] D. Jansen, Ch. Stabler, F. Goetz-Neunhoeffer, S. Dittrich, J. Neubauer, Does ordinary Portland cement contain amorphous phase? A quantitative study using an external standard method, Powder Diffract. 26 (2011) 31–38, https://doi.org/10.1154/1.3549186.
[12] D. Jansen, F. Goetz-Neunhoeffer, Ch. Stabler, J. Neubauer, A remastered external standard method applied to the quantification of early OPC hydration, Cem. Concr. Res. 41 (2011) 602–608, https://doi.org/10.1016/j.cemconres.2011.03.004.
[13] D. Jansen, F. Goetz-Neunhoeffer, B. Lothenbach, J. Neubauer, The early hydration of Portland cement (OPC): an approach comparing measured heat flow with calculated heat flow from QXRD, Cem. Concr. Res. 42 (2012) 134–138, https://doi.org/10.1016/j.cemconres.2011.09.001.
[14] D. Jansen, Ch. Naber, D. Ectors, Z. Lu, X.M. Kong, F. Goetz-Neunhoeffer, J. Neubauer, The early hydration of OPC investigated by in-situ XRD, heat flow calorimetry, pore water analysis and ^{1}H NMR: learning about adsorbed ions from a complete mass balance approach, Cem. Concr. Res. 109 (2018) 230–242, https://doi.org/10.1016/j.cemconres.2018.04.017.
[15] Y. Yue, J.J. Wang, P.A. Muhammed Basheer, Y. Bai, In-situ monitoring of early hydration of clinker and Portland cement with optical fiber excitation Raman spectroscopy, Cem. Concr. Compos. 112 (2020) 103664, https://doi.org/10.1016/j.cemconcomp.2020.103664.
[16] T. Mi, Y. Li, W. Liu, W. Li, W. Long, Z. Dong, Q. Gong, F. Xing, Y. Wang, Quantitative evaluation of cement paste carbonation using Raman spectroscopy, Mat. Degradation 5 (2021) 35, https://doi.org/10.1038/s41529-021-00181-6.
[17] R. Ylmèn, U. Jäglid, I. Panas, Monitoring early hydration of cement by ex situ and in situ ATR-FTIR – a comparative study, J. Am. Ceram. Soc. 97 (2014) 3669–3675, https://doi.org/10.1111/jace.13186.
[18] J. Kalkreuth, A. Ullrich, K. Garbev, D. Merz, P. Stemmermann, D. Stapf, Accelerated carbonation of hardened cement paste: quantification of calcium carbonate via ATR infrared spectroscopy, J. Am. Ceram. Soc. 107 (4) (2023), https://doi.org/10.1111/jace.19546, 2627–1640.
[19] V.H.J. Mendes dos Santos, D. Pontin, G.G.D. Ponzi, A.S. de Guimarães e Stepanha, R.B. Martel, M.K. Schütz, S.M.O. Einloft, F. Dalla Vecchia, Application of Fourier transform infrared spectroscopy (FTIR) coupled with multivariate regression for calcium carbonate ($CaCO_3$) quantification in cement, Constr. Build. Mater. 313 (2021) 125413, https://doi.org/10.1016/j.conbuildmat.2021.125413.
[20] J. Higl, D. Hinder, C. Rathgeber, B. Ramming, M. Lindèn, Detailed in situ ATR-FTIR spectroscopy study of the early stages of C-S-H formation during hydration of monoclinic C_3S, Cem. Concr. Res. 142 (2021) 106367, https://doi.org/10.1016/j.cemconres.2021.106367.
[21] E. Pustovgar, R.P. Sangodkar, A.S. Andreev, M. Palacios, B.F. Chmelka, R.J. Flatt, J. B. d'Espinose de Lacaillerie, Understanding silicate hydration from qhantitative analysis of hydrating tricalcium silicates, Nat. Commun. 7 (2016) 10952.
[22] E. John, D. Stephan, Calcium silicate hydrate - in-situ development of the silicate structure followed by infrared spectroscopy, J. Am. Ceram. Soc. 104 (2021) 6611–6624, https://doi.org/10.1111/jace.18019.
[23] H.F.W. Taylor, Cement Chemistry, second edition, Thomas Telford Publishing, London, 1997.
[24] K. Garbev, B. Gasharova, A. Ullrich, G. Beuchle, P. Stemmermann, Assignment of Si-O vibrational modes in the IR spectra of C-S-H phases based on single crystal polarized IR and Raman spectra of 14Å Tobermorite, Jennite and Jaffeite, Cem. Concr. Res. 198 (2025) 108000, https://doi.org/10.1016/j.cemconres.2025.108000.
[25] S. Brunauer, P. Emmett, E. Teller, Adsorption of gases in multimolecular layers, J. Am. Chem. Soc. 60 (1938) 309–319, https://doi.org/10.1021/ja01269a023.
[26] O. Burgos-Montes, M. Palacios, P. Rivilla, F. Puertas, Compatibility between superplasticizer admixtures and cements with mineral additions, Constr. Build. Mater. 31 (2012) 300–309, https://doi.org/10.1016/j.conbuildmat.2011.12.092.
[27] F. Andersen, L. Brečević, G. Beuter, D. Dell'amico, F. Calderazzo, N. Bjerrum, A. Underhill, Infrared spectra of amorphous and crystalline calcium carbonate, Acta Chem. Scand. 45 (1991) 1018–1024, https://doi.org/10.3891/ACTA.CHEM.SCAND.45-1018.
[28] M. Król, A. Koleżyński, P. Florek, P. Jeleń, D. Kozień, W. Mozgawa, Full spectroscopic characterization of clinker minerals (anhydrous cement), J. Mol. Struct. 1255 (5) (2022) 132454, https://doi.org/10.1016/j.molstruc.2022.132454.
[29] V. Timon, D. Torrens-Martin, L.J. Fernández-Carrasco, S. Martínez-Ramírez, Infrared and Raman vibrational modelling of β-C_2S and C_3S compounds, Cem. Concr. Res. 169 (2023) 107162, https://doi.org/10.1016/j.cemconres.2023.107162.
[30] M. Horgenies, J.J. Chen, C. Bouillon, Overview about the use of Fourier transform infrared spectroscopy to study cementitious materials, in: WIT Transactions on Engineering Sciences, Materials Characterization VI 77, 2013, pp. 251–262, https://doi.org/10.2495/MC130221.
[31] Y. Liu, A. Wang, J.J. Freemann, RAMAN, MIR, AND NIR SPECTROSCOPIC STUDY OF CALCIUM SULFATES: GYPSUM, BASSANITE, AND ANHYDRITE, in: 40th Lunar and Planetary Science Conference, 2009. Washington. 2009LPI....40.2128L.
[32] L. Fernandez-Carrasco, D. Torrens-Martin, L.M. Morales, S. Martinez-Ramirez, Infrared spectroscopy in the analysis of building and construction materials, infrared spectroscopy-materials science, Eng. Technol. (2012) 369–382, https://doi.org/10.5772/36186.
[33] M.Y.A. Mollah, W. Yu, R. Schennach, D.L. Cocke, A Fourier transform infrared spectroscopic investigation of the early hydration of Portland cement and the influence of sodium lignosulfonate, Cem. Concr. Res. 30 (2000) 267–273, https://doi.org/10.1016/S0008-8846(99)00243-4.
[34] L. Black, A. Stumm, K. Garbev, P. Stemmermann, K.R. Hallam, G.C. Allen, X-ray photoelectron spectroscopy of the cement clinker phases calcium trisilicate and β-calcium disilicate, Cem. Concr. Res. 33 (1) (2003) 1561–1565, https://doi.org/10.1016/S0008-8846(03)00097-8.
[35] E.T. Rodriguez, K. Garbev, D. Merz, L. Black, I.G. Richardson, Thermal stability of C-S-H phases and applicability of Richardson and Groves' and Richardson C-(A)-S-

H(I) models to synthetic C-S-H, Cem. Concr. Res. 93 (2017) 45–56, https://doi.org/10.1016/j.cemconres.2016.12.005.
[36] Y. Yan, B. Ma, G.D. Miron, D.A. Kulik, K. Scrivener, B. Lothenbach, Al uptake in calcium silicate hydrate and the effect of alkali hydroxide, Cem. Concr. Res. 162 (2022) 106957, https://doi.org/10.1016/j.cemconres.2022.106957.
[37] C. Jakob, D. Jansen, N. Ukrainczyk, E. Koenders, U. Pott, D. Stephan, J. Neubauer, Relating Ettringite formation and rheological changes during the initial cement hydration: a comparative study applying XRD analysis, rheological measurements and modeling, Materials 12 (2019) 2957, https://doi.org/10.3390/ma12182957.
[38] D. Gastaldi, F. Canonico, E. Boccaleri, Ettringite and calcium sulfoaluminate cement: investigation of water content by near-infrared spectroscopy, J. Mater. Sci. 44 (2009) 5788–5794, https://doi.org/10.1007/s10853-009-3812-1.
[39] P.M. Dove, J.D. Rimstidt, Silica Water Interactions, in: Silica Reviews in Mineralogy, Mineral. Society of America 29, 1994, pp. 259–307.
[40] B.A. Morrow, I.A. Cody, Infrared studies of reactions on oxide surfaces. 6. Active sites on dehydroxylated silica for the chemisorption of ammonia and water, J. Phys. Chem. 80 (18) (1976) 1998–2004, https://doi.org/10.1021/j100559a010.
[41] W. Mosgawa, M. Handke, W. Jastrzębski, Vibrational spectra of aluminosilicate structural clusters, J. Mol. Struct. 704 (2004) 247–257, https://doi.org/10.1016/j.molstruc.2004.01.059.
[42] C. Marcolli, G. Calzaferi, Vibrational structure of monosubstituted octahydrosilasesquioxanes, J. Phys. Chem. B 101 (1997) 4925–4933. http://hdl.handle.net/2027.42/34737.
[43] C. Eypert-Blaison, L.J. Michot, B. Humbert, M. Pellentier, F. Villiéras, J.B. d'Espinose de la Caillerie, Hydration Water and Swelling Behavior of Magadiite. The H^+, Na^+, K^+, Mg^{2+}, and Ca^{2+} exchanged forms, J. Phys. Chem. B 106 (2002) 730–742, https://doi.org/10.1021/cm001130+.
[44] G.L. Kalousek, Discussion on influence of gypsum on Portland cement, in: W. Lerch (Ed.), Proceedings of the 49th annual meeting of the American society for testing materials 24–28, 1946, pp. 1293–1297.
[45] M. Henry, Retrosynthesis in inorganic crystal structures: application to nesosilicate and inosilicate networks, Coord. Chem. Rev. 178-180 (2) (1998) 1109–1163, https://doi.org/10.1016/S0010-8545(98)00167-2.
[46] B.A. Morrow, A. Devi, Adsorption of water and 18 O exchange of surface hydroxyl groups on silica, Can. J. Chem. 48 (1970) 2454–2456, https://doi.org/10.1139/v70-416.
[47] J.E. Del Bene, K. Runge, R.J. Bartlett, A quantum chemical mechanism for the water-initiated decomposition of silica, Comput. Mater. Sci. 27 (2003) 102–108, https://doi.org/10.1016/S0927-0256(02)00432-9.
[48] J.D. Ortego, Y. Barroeta, F.K. Cartledge, H. Akhter, Leaching effects on silicate polymerization. An FTIR and ^{29}Si NMR study of Lead and zinc in Portland cement, Environ. Sci. Technol. 25 (1991) 1171, https://doi.org/10.1021/es00018a024.
[49] P. Yu, B. Poe, P. McMillan, Structure of calcium silicate hydrate (C-S-H): near-, mid-, and far-infrared spectroscopy, J. Am. Min. Soc. 82 (3) (2004) 742–748, https://doi.org/10.1111/j.1151-2916.1999.tb01826.x.